This article has been accepted for publication in a future issue of this journal, but has not been fully edited. Content may change prior to final publication.
Citation information: DOI: 10.1109/TIE.2025.3572980, IEEE Transactions on Industrial Electronics

Intelligent Diagnosis of Closed-Loop Motor Drives Using Interior Control Signals under Industrial Low Sampling Rate Conditions

Jinze Jiang, Yaguo Lei, *Senior Member*, *IEEE*, Zidong Wang, *Fellow*, *IEEE*, Ke Feng, *Member*, *IEEE*, and Xiaofei Liu

***Abstract*—Interior control signals derived from motor controllers have gained increasing attention in closed-loop motor drive systems for interturn short-circuit fault diagnosis. Mainstream diagnosis methods generally rely on the extraction of control signals within experimental settings featuring high sampling rates, such as 10 kHz or 40 kHz. However, in practical engineering, the industrial sampling rate of control signals typically reaches only 1 kHz or even lower. This limitation makes it challenging for control signals to intuitively distinguish between healthy and faulty states. To address this practical constraint, an intelligent diagnosis method, termed the prior knowledge integrated contrastive diagnosis model (PK-CDM), is proposed. First, space voltage vectors of interior control signals are extracted as inputs of the PK-CDM to detect the interturn short circuit in a closed-loop motor drive system. Second, the physical variation regularity of space voltage vectors is formulated as the prior diagnostic knowledge to compensate for the lack of information under low sampling rate conditions. Finally, a contrastive pre-training strategy is employed to facilitate the construction of the PK-CDM at an industrially low sampling rate. Experimental results demonstrated that the proposed PK-CDM solves the issue of information loss under industrial low sampling rate conditions by integration of prior diagnostic knowledge with a contrastive learning strategy, thereby yielding superior diagnostic accuracy compared to other state-of-the-art (SOTA) methods.**

***Index Terms*—Intelligent diagnosis, electrical faults, closed-loop motor drives, interior control signals, low sampling rate.**

I. Introduction

As the core component of high-end equipment such as industrial robots, the closed-loop motor drive serves as a typical electromechanical carrier, encompassing an electrical machine, a motor controller, and an inverter [1]. Unlike open-loop motor drives, closed-loop motor drives can compensate for system asymmetry through the regulating effect of closed-loop control, thereby ensuring operational stability [2]. Given their critical importance in industrial applications, the reliability and safety of closed-loop motor drives have become a focal point of extensive research [3].

In the field of closed-loop motor drive diagnosis, interturn short-circuit faults (ISCFs) in motor stators pose one of the most critical challenges to the operational reliability, primarily due to their high occurrence probability, weak incipient fault signatures and propensity for rapid progression to phase-to-phase or phase-to-ground faults under continuous operation. The primary challenge lies in addressing the issue that the regulating effect of closed-loop control alters behaviors of ISCFs and complicates the diagnosis procedure. This regulating mechanism operates by having the motor controller enforce balanced phase currents and suppress any additional negative-sequence components caused by ISCFs or other electrical faults [4]. The impact of closed-loop control on rotor fault diagnosis in induction motor drive systems has been explored in [5], with findings demonstrating that the straightforward application of the motor current signature analysis is rendered ineffective. In [6], a comparative study utilizing different monitoring signals for a stator FOC drive system revealed that closed-loop control impedes the efficient detection of stator high-resistance connection faults. Consequently, the regulating effect of closed-loop control prevents traditional monitoring signals from accurately representing diagnostic information, leading to incorrect identification of the true state of the faulty device.

Current research on ISCF diagnosis in closed-loop motor drives has demonstrated substantial advancements in incipient ISCF detection capabilities under diverse control schemes. In [7], the third harmonic component of stray flux was employed for ISCFs diagnosis in field-oriented control (FOC) drive systems, facilitating accurate fault coil localization through the

Manuscript received Month xx, 2xxx; revised Month xx, xxxx; accepted Month x, xxxx. This work was supported in part by the National Key R&D Program of China under Grant 2022YFB3402100, in part by the Key Program of the National Natural Science Foundation of China under Grant 52435003, in part by the National Science Fund for Distinguished Young Scholars of China under Grant 52025056, in part by Shaanxi Science and Technology Innovation Team under Grant 2023-CX-TD-15, in part by the Sanqin Scholar Innovation Team and in part by the Fundamental Research Funds for the Central Universities.

J. Jiang, K. Feng, and X. Liu are with the Key Laboratory of Education Ministry for Modern Design and Rotor-Bearing System, Xi'an Jiaotong University, Xi'an, Shaanxi 710049, China. (e-mail: jiangjinze @stu.xjtu.edu.cn; kefeng@xjtu.edu.cn; 4120101099@stu.xjtu.edu.cn).

Y. Lei is with the Key Laboratory of Education Ministry for Modern Design and Rotor-Bearing System, Xi'an Jiaotong University, Xi'an, Shaanxi 710049, China. (Corresponding author contacts, e-mail: yaguolei@mail.xjtu.edu.cn).

Zidong Wang is with the Department of Computer Science, Brunel University London, UB8 3PH Uxbridge, U.K. (e-mail: Zidong.Wang@brunel.ac.uk).

This article has been accepted for publication in a future issue of this journal, but has not been fully edited. Content may change prior to final publication. Citation information: DOI: 10.1109/TIE.2025.3572980, IEEE Transactions on Industrial Electronics

installation of a fluxgate sensor. In [8], an external magnetic loop antenna was used to detect ISCFs in direct torque control (DTC) drive systems, and the harmonics in the measured flux leakage spectrum were proposed as fault signatures containing abundant diagnostic information. In [9], a discrete wavelet transform method was introduced to extract fault features from the cost function, which enables ISCF diagnosis in model predictive current control (MPCC) drive systems without additional monitoring signals. Moreover, in [10], a generalized ISCF detection method was proposed with the $\alpha\beta$-axis current residuals, achieving independence from cost functions and exhibiting compatibility with both MPCC and model predictive torque control (MPTC). However, the practical implementation of these methods is significantly constrained by the narrow applicability to specific control schemes or the necessity for supplementary sensing devices.

Given the sensorless and non-invasive characteristics of interior control signals [11], researchers have explored how these advantages can mitigate the influence of closed-loop control and enhance the diagnosis of closed-loop motor drives. In [12], the constant component and the double-fundamental harmonic component of internal signals were employed for ISCF diagnosis in direct FOC drives, exhibiting superiority over classical motor current signature analysis (MCSA) methods. In [13], an adaptive nonlinear diagnostic model using a self-recurrent wavelet neural network was introduced for multi-phase motor drives. This model utilized gate signals collected from motor controllers as inputs to identify open switch faults in less than 1 ms without extra sensors. In [14], a novel indicator was presented to enhance the robustness of ISCF detection in permanent magnet synchronous motor (PMSM) drive systems under varying controller bandwidths. This method incorporated the second harmonics of control currents and voltages with the Rayleigh quotient function. In [15], it is demonstrated that space voltage vectors obtained from a motor controller are effective for diagnosing ISCFs in closed-loop motor drives with FCS-MPC. This method utilized controller outputs as a fault indicator, exhibiting universal applicability for diverse control schemes. Furthermore, several popular deep learning models were constructed in [16], using statistical data of space voltage vectors as inputs for the diagnostic models. The integration of deep neural networks has mitigated the negative impact of operational conditions on ISCF diagnosis, thereby enhancing the diagnostic efficiency.

While the feasibility of using interior control signals for ISCF diagnosis without interference from closed-loop control has been established, existing research has overlooked challenges arising from industrial low sampling rates. Most studies on electrical fault diagnosis for closed-loop motor drives assume the availability of high sampling rates for interior control signals, such as 10 kHz or 40 kHz [12]-[16]. However, due to actual limitations in communication bandwidth and hardware costs, the sampling rate of interior control signals for industrial robots and other typical applications typically only reaches 1 kHz or even lower. In [17], the torque signal from a motor controller in a 6-degree of freedom (DOF) industrial welding robot was employed for the gearbox fault detection at a sampling rate of 1 kHz. In [18], for the operation safety of a wafer transfer robot with five axes, current and velocity signals

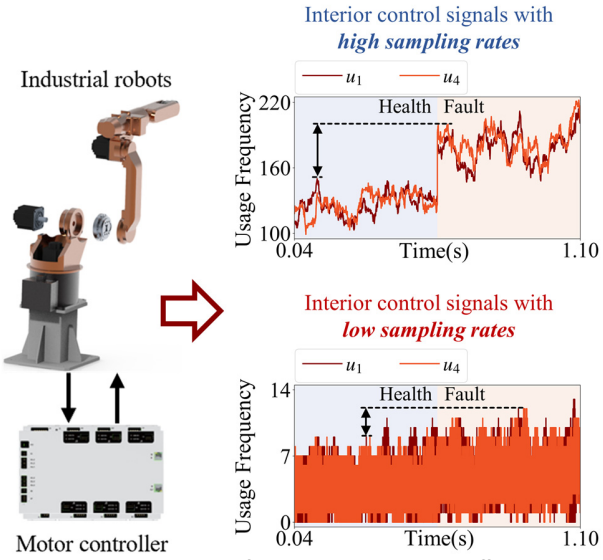

Fig. 1. Interior control signal of industrial robots under different sampling rates and its amplitude changes.

were extracted from motor controllers at 1 kHz to enable fault diagnosis of harmonic drive and timing belt components. It is noteworthy that a low sampling rate in interior control signal acquisition may lead to signal distortion and information loss, impeding the accurate fault diagnosis through signal analysis. The impact of different sampling rates on usage frequencies of space voltage vectors from a motor controller of industrial robots is depicted in Fig. 1. At a high sampling rate, usage frequencies of space voltage vectors in a fault state are significantly higher than in a healthy state. However, as the sampling rate decreases, the information loss occurs in these statistics calculated over the whole operation period, causing a notable reduction in the amplitude difference. At a low sampling rate, distinguishing between healthy and faulty data becomes challenging, rendering traditional diagnosis methods ineffective. Thus, it is essential to develop a closed-loop motor drive diagnosis method capable of utilizing interior control signals at low sampling rates for industrial applications.

Early works on fault diagnosis at a low sampling rate have concentrated on developing novel signal processing methods that are insensitive to the reduction in sampling rates, fulfilling practical requirements for industrial deployment. In [19], the integration of a digital notch filter with discrete-time Fourier transform and autoregressive-based spectrum methods enabled the effective detection of broken rotor bar (BRB) faults in induction motors (IMs) at low sampling rates. In [20], the stationary wavelet packet transform (SWPT) was employed for feature extraction from current signals, significantly improving the diagnostic accuracy of BRB faults in IMs at low sampling rates. As operational conditions become complex, the impact of information loss and signal distortion caused by low sampling rates on fault diagnosis accuracy has become more pronounced, rendering signal processing methods ineffective. Although the potential of deep learning methods has been proven in fault diagnosis for power electronics and other fields [21]-[25], mature SOTA methods have poor robustness to complex working conditions at low sampling rates. Few studies have introduced novel deep learning-based diagnosis methods to address the issue of fault information loss at low sampling rates.

This article has been accepted for publication in a future issue of this journal, but has not been fully edited. Content may change prior to final publication. Citation information: DOI: 10.1109/TIE.2025.3572980, IEEE Transactions on Industrial Electronics

In [26], a generative adversarial network (GAN) was used to enhance the original coding data of arc faults at low sampling rates, combined with an adaptive asymmetric convolutional neural network to improve the fault feature extraction ability. In [27], a deep residual architecture with a feature-sharing mechanism was proposed, achieving accurate motor bearing fault diagnosis even when the sampling rate of vibration signals was reduced to one-fourth of the original. Recent research on ISCF diagnosis in closed-loop motor drives using interior control signals has overlooked the low sampling rate constraint. Their sampling rates in industrial applications are reduced to 1/10 or 1/40 of those achievable in laboratory settings, posing significant challenges for incipient ISCF diagnosis. To address this issue, an intelligent method known as the prior knowledge integrated contrastive diagnosis model (PK-CDM) is proposed. This method uses space voltage vectors of interior control signals to mitigate the effects of closed-loop control. Then, the physical variation regularity of these vectors is formulated as prior diagnostic knowledge to counteract the information loss inherent at low sampling rates. To further enhance diagnostic accuracy within industrial low sampling rate constraints, a contrastive pre-training strategy is applied, incorporating data augmentation techniques and a hybrid contrastive loss function to aid in the construction of the PK-CDM.

The main contributions of this paper are as follows:

1) An intelligent prior knowledge integrated contrastive diagnosis model (PK-CDM) is introduced for diagnosing electrical faults in closed-loop motor drives. The variation regularity of control signals is formulated and represented through a fully-connected prior knowledge integrated subnetwork, enabling the observation of more valuable information even at industrial low sampling rates.

2) Space voltage vectors extracted from a motor controller are employed as inputs for the proposed PK-CDM, with an analysis of the impact of closed-loop control on fault information extraction. Fault diagnosis unaffected by closed-loop influences is accomplished by sampling and monitoring changes in the duration of space voltage vectors.

3) A contrastive pre-training strategy is applied to develop the fault feature encoder, which maximizes the distinction between healthy and faulty states under industrial low sampling rate conditions. Besides, tailored data augmentation methods and a hybrid contrastive loss function are designed to enhance the utilization of restricted information at low sampling rates.

The remainder of this paper is organized as follows. Section II introduces challenges of electrical fault diagnosis for closed-loop motor drives at low sampling rates. Section III provides a detailed explanation of the proposed PK-CDM. In Section IV, the superiority of the PK-CDM is experimentally validated. Finally, Section V presents the conclusion.

II. Challenges of Electrical Fault Diagnosis at Low Sampling Rates

In this section, space voltage vectors from a motor controller are utilized as a substitute for traditional monitoring signals to diagnose ISCFs in closed-loop motor drives, thereby avoiding the adverse effects of closed-loop control. Then, the problem of industrial low sampling rates is discussed when using space voltage vectors for the closed-loop motor drive diagnosis.

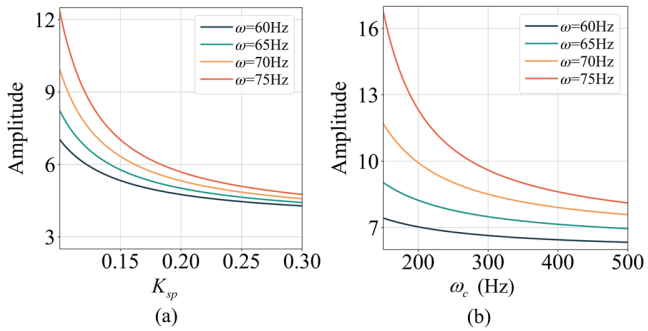

Fig. 2. Amplitude variations of fault components in current signals under different control parameters. (a) Amplitude variations under different proportional terms. (b) Amplitude variations under different bandwidths.

A. Regulating Effect of Closed-Loop Control

The regulating effect of closed-loop control is exemplified using an incipient ISCF, which represents one of the most significant electrical faults in motor drives. Incipient ISCFs can be modeled as disturbances to the motor's electromagnetic torque [28], [29] and analyzed using transfer functions of the motor drive system within the synchronous reference frame.

The closed-loop transfer function of the current loop is defined by (1). Then, the transfer function relating the q-axis current i_q to the torque disturbance T_m can be derived as in (2):

$$G_{c\_I}(s)=\frac{K_{cp}}{1.5T_sLs^2+Ls+K_{cp}}\approx\frac{\omega_c}{s+\omega_c} \tag{1}$$

$$G_{i_q\_T_m}(s)=\frac{i_q(s)}{T_m(s)}=\frac{K_{sp}K_{vf}(\tau_s s+1)}{J_m\tau_s s^2(s/\omega_c+1)+K_tK_{sp}K_{vf}(\tau_s s+1)} \tag{2}$$

where ω_c is the bandwidth of a current loop controller, K_{sp} is the proportional term of a speed loop controller, τ_s is the integral term, J_m is the motor inertia parameter, K_{vf} is the feed-back gain constant, and K_t is the motor torque constant.

$$G_{i_q\_T_m}(j\omega)=\frac{K_{sp}K_{vf}\tau_s j\omega+K_{sp}K_{vf}}{j(-J_m\tau_s\omega^3/\omega_c+K_tK_{sp}K_{vf}\tau_s\omega)+(-J_m\tau_s\omega^2+K_tK_{sp}K_{vf})} \tag{3}$$

$$\left|G_{i_q\_T_m}(\omega)\right|=\frac{K_{sp}K_{vf}\sqrt{\tau_s^2\omega^2+1}}{\sqrt{(-J_m\tau_s\omega^3/\omega_c+K_tK_{sp}K_{vf}\tau_s\omega)^2+(-J_m\tau_s\omega^2+K_tK_{sp}K_{vf})^2}} \tag{4}$$

Frequency-response analysis is applied to evaluate the transfer functions in (3) and (4). The values of τ_s, J_m, K_{vf} and K_t in (4) are determined according to [30]. The order of the numerator and denominator indicates that the system possesses filtering capabilities, resulting in the suppression of fault components caused by ISCFs within motor current signals.

Based on this frequency-response analysis, the amplitude variation of ISCF components within motor current signals under different control parameters is depicted in Fig. 2. When comparing Fig. 2 (a) with Fig. 2 (b), the results across various operating frequencies demonstrate that the amplitude variation tendency decreases significantly with changes in closed-loop control parameters. Thus, the regulating effect of closed-loop control masks valuable information, thereby impeding the extraction of electrical fault signatures from motor currents.

This article has been accepted for publication in a future issue of this journal, but has not been fully edited. Content may change prior to final publication. Citation information: DOI: 10.1109/TIE.2025.3572980, IEEE Transactions on Industrial Electronics

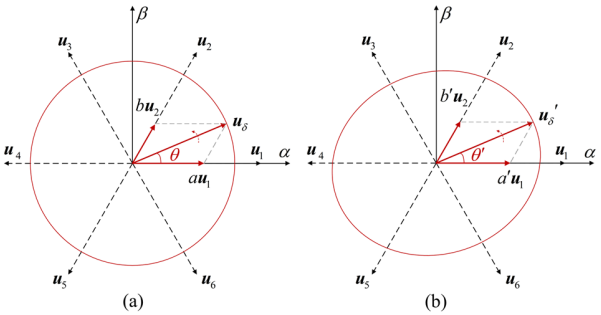

Fig. 3. Motion trajectory of space voltage vector in the *α-β* reference frame. (a) Health state. (b) Fault state.

B. Electrical Fault Diagnosis by Space Voltage Vectors

Given the negative impact of the closed-loop control scheme on extracting fault information from motor currents, space voltage vectors derived from a motor controller are proposed as an alternative approach for achieving electrical fault diagnosis in closed-loop motor drives.

$$\begin{bmatrix} \boldsymbol{u}_\alpha(t) \\ \boldsymbol{u}_\beta(t) \\ \boldsymbol{u}_0(t) \end{bmatrix} = \frac{2}{3}\begin{bmatrix} 1 & -1/2 & -1/2 \\ 0 & \sqrt{3}/2 & -\sqrt{3}/2 \\ 1/2 & 1/2 & 1/2 \end{bmatrix}\begin{bmatrix} \boldsymbol{u}_a(t) \\ \boldsymbol{u}_b(t) \\ \boldsymbol{u}_c(t) \end{bmatrix} \tag{5}$$

Suppose that $\boldsymbol{u}_a(t)$, $\boldsymbol{u}_b(t)$, and $\boldsymbol{u}_c(t)$ are phase voltages of a closed-loop motor drive. In (5), the representation of these signals in the *α-β* reference frame can be obtained by the application of Clark transformation [31].

Then, the space voltage vector $\boldsymbol{u}_\delta(t)$ can be defined in the *α-β* reference frame in (6):

$$\begin{aligned} \boldsymbol{u}_\delta(t) &= \boldsymbol{u}_\alpha(t) + j\boldsymbol{u}_\beta(t) \\ &= \frac{2}{3}\left[\boldsymbol{u}_a(t) + \boldsymbol{u}_b(t)e^{j2\pi/3} + \boldsymbol{u}_c(t)e^{j4\pi/3}\right] \\ &= \sqrt{2}u_m e^{j\theta} \end{aligned} \tag{6}$$

where u_m is the peak value of phase voltages and θ is the rotation angle of space voltage vectors.

As shown in Fig.3, the motion trajectory of space voltage vector $\boldsymbol{u}_\delta(t)$ is circular at the health state, and its trajectory transforms into an elliptical shape affected by ISCFs [32].

$\boldsymbol{u}_\delta(t)$ can be decomposed into the combination of two adjacent basic voltage vectors, such as $\boldsymbol{u}_1(t)$ and $\boldsymbol{u}_2(t)$. During one electrical period T_c, the integral of decomposed voltage vectors by time satisfies the following formula:

$$\int_0^{T_c} \boldsymbol{u}_\delta(t)dt = \int_0^{aT_c} \boldsymbol{u}_1(t)dt + \int_0^{bT_c} \boldsymbol{u}_2(t)dt + \int_0^{cT_c} \boldsymbol{0}dt \tag{7}$$

where $\boldsymbol{0}$ is the zero-voltage vector, *a*, *b* and *c* are the duty ratio of basic voltage vectors and a zero voltage vector respectively. The angle between two adjacent basic voltage vectors is $\pi/3$.

In the *α-β* reference frame, the vector norm of $\boldsymbol{u}_\delta(t)$ has the following relationship with $\boldsymbol{u}_1(t)$ and $\boldsymbol{u}_2(t)$:

$$\begin{cases} |\boldsymbol{u}_\delta(t)|\cos\theta = a|\boldsymbol{u}_1(t)| + b|\boldsymbol{u}_2(t)|\cos(\pi/3) \\ |\boldsymbol{u}_\delta(t)|\sin\theta = b|\boldsymbol{u}_2(t)|\sin(\pi/3) \end{cases} \tag{8}$$

$$\begin{cases} T_1' = a'T_c = \dfrac{\sqrt{3}|\boldsymbol{u}_\delta(t)|}{u_{dc}} T_c \sin(\dfrac{\pi}{3} - \theta) \\ T_2' = b'T_c = \dfrac{\sqrt{3}|\boldsymbol{u}_\delta(t)|}{u_{dc}} T_c \sin(\theta) \end{cases} \tag{9}$$

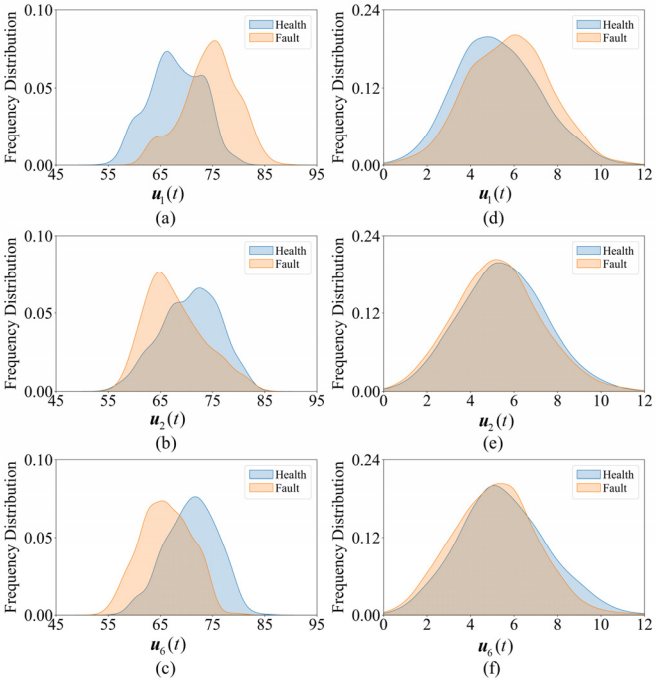

Fig. 4. Distribution discrepancy of space voltage vectors at healthy and faulty states at different sampling rates. (a) $\boldsymbol{u}_1$ at high sampling rates. (b) $\boldsymbol{u}_2$ at high sampling rates. (c) $\boldsymbol{u}_6$ at high sampling rates. (d) $\boldsymbol{u}_1$ at low sampling rates. (e) $\boldsymbol{u}_2$ at low sampling rates. (f) $\boldsymbol{u}_6$ at low sampling rates.

Letting the norm of the basic voltage vector $\boldsymbol{u}_1(t)$ and $\boldsymbol{u}_2(t)$ be two-thirds of the system bus voltage u_{dc}, the duration of basic voltage vectors can be calculated in (9).

Based on the above decomposition principle of space voltage vectors, the motion trajectory change caused by ISCFs can be represented by the duration change. Thus, the non-intrusive ISCF diagnosis for closed-loop motor drives without the negative effect of closed-loop control can be realized by sampling and monitoring the duration change of space voltage vectors at health and fault states.

C. Problem Statement of Low Sampling Rates

In the discrete sampling process of space voltage vectors obtained from a motor controller, the duration changes of space voltage vectors can be characterized by their usage frequencies within each operational period. Consequently, the issue of industrial low sampling rates can be described by observing changes in the statistical distribution of usage frequencies.

Fig. 4 illustrates the statistical distribution of the basic voltage vector $\boldsymbol{u}_1(t)$ alongside its adjacent basic voltage vectors $\boldsymbol{u}_2(t)$ and $\boldsymbol{u}_6(t)$ when an ISCF occurs in phase A of the motor stator. In this figure, the horizontal coordinate represents the usage frequency recorded over a unit operational period, while the vertical coordinate denotes the probability of the frequency distribution. A comparative analysis of Fig. 4 (a), Fig. 4 (b) and Fig. 4 (c) reveals that the occurrence of ISCFs leads to a rise in the mean value of frequency distribution for $\boldsymbol{u}_1(t)$, whereas $\boldsymbol{u}_2(t)$ and $\boldsymbol{u}_6(t)$ exhibit opposing changes at a high sampling rate. These observations are consistent with the decomposition mechanism of space voltage vectors, providing a fault indicator for ISCF detection. However, as shown in Fig. 4 (d), Fig. 4 (e), and Fig. 4 (f), the usage frequency recorded over a single operational cycle is significantly reduced, and the statistical distribution discrepancies between healthy and fault states

This article has been accepted for publication in a future issue of this journal, but has not been fully edited. Content may change prior to final publication. Citation information: DOI: 10.1109/TIE.2025.3572980, IEEE Transactions on Industrial Electronics

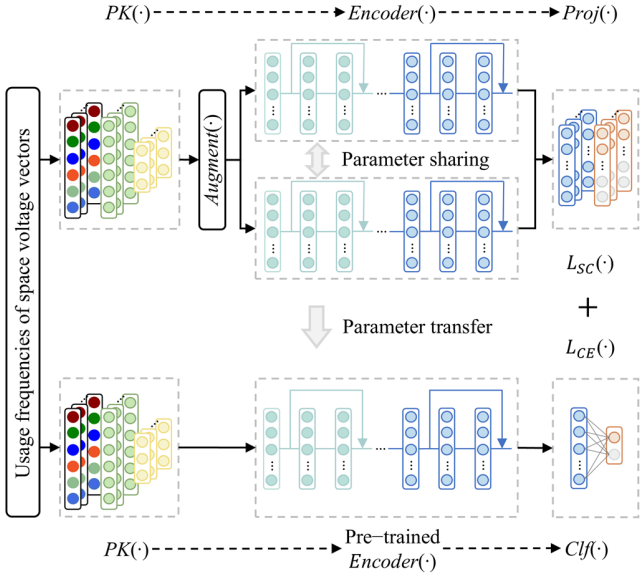

Fig. 5. The architecture of proposed PK-CDM.

weaken at lower sampling rates. Consequently, the issue of low sampling rates results in the information loss of space voltage vectors, hindering information extraction by diagnostic models.

III. Intelligent Diagnosis Method under Industrial Low Sampling Rate Conditions

In this section, to address the challenge of diagnosing closed-loop motor drives at industrial low sampling rates, a novel PK-CDM method is depicted in Fig. 5. Initially, the usage frequencies of space voltage vectors serve as inputs for a prior knowledge integrated subnetwork, fusing correlation changes among space voltage vectors to mitigate information loss. In the contrastive representation learning branch, a contrastive pre-training strategy is introduced to extract fault features, thereby enhancing intra-class similarity and amplifying inter-class dissimilarity. Finally, the diagnostic classifier learning branch aims to construct a binary classifier based on the pre-trained encoder, aligning with the requirements of electrical fault diagnosis tasks.

A. Prior Knowledge Integrated Subnetwork

The mechanism analysis presented in Section II demonstrates that when ISCFs occur, the trajectory of space voltage vectors transitions from a circular to an elliptical shape. The long axis of this elliptical fault trajectory aligns with the direction of the basic voltage vector associated with the faulty phase.

Take the occurrence of ISCFs in the motor phase A as an example. The long axis of this space voltage vector trajectory tends to the direction of $\boldsymbol{u}_1(t)$ and $\boldsymbol{u}_4(t)$, extending their duration. Based on the decomposition principle of space voltage vectors in Section II, when the duration of $\boldsymbol{u}_1(t)$ increases, the duration of adjacent voltage vectors $\boldsymbol{u}_2(t)$ and $\boldsymbol{u}_6(t)$ will decrease, which is also verified in Fig. 4. Thus, when ISCFs occur, the prior knowledge about correlation changes between space voltage vectors can be formulated as follows:

$$\boldsymbol{u}_{i\_fus}(t)' = \sum_i \frac{\omega_i}{\sum_m \omega_m} \boldsymbol{u}_i(t) \tag{10}$$

$$\boldsymbol{u}_p(t)' = \boldsymbol{u}_{i\_fus,p+}(t)' + \boldsymbol{u}_{i\_fus,p-}(t)' \tag{11}$$

where $\boldsymbol{u}_i(t)$ is the original basic voltage vector and ω_i is the correlation weight. m is the index of the mth related space voltage including the original basic voltage vector, while ω_m represents the corresponding weight for each vector. Hence, the fusion representation $\boldsymbol{u}_{i\_fus}(t)'$ of correlation changes is computed by the weight summation and normalization of the basic voltage and their adjacent vectors. Then, $\boldsymbol{u}_{i\_fus,\,p+}(t)'$ and $\boldsymbol{u}_{i\_fus,\,p-}(t)'$ are the positive and negative fusion vectors in the same phase, representing the fault state of corresponding motor stator coil in (11) corporately.

The prior knowledge of space voltage vectors formulated by (10) and (11) can be expressed by a fully-connected network to construct a prior knowledge integrated subnetwork *PK* (·). In this subnetwork, the fused weights of space voltage vectors are represented by the learnable parameters, endowing the vector fusion process with adaptive optimization. Therefore, this subnetwork is able to observe the correlation change between space voltage vectors from a global perspective to extract more fault information, and solve the problem of industrial low sampling rates without excessive addition of model size.

B. Contrastive Representation Learning Branch

This branch includes three core components: data augmentation methods *Augment* (·), a feature encoder module *Encoder* (·) and a supervised contrastive loss $L_{\mathrm{sc}}(\cdot)$.

Augment (·): Based on the data augmentation principle that cannot change the semantic meaning of raw inputs [33], three methods, Gaussian noise, random scaling and mask noise, are used to supplement the insufficiency of useful information for space voltage vectors under low sampling rate scenarios.

Let $i \in I \equiv \{1 \ldots 2N\}$ be the index of raw and augmented input $\boldsymbol{u}_i$ of space voltage vector datasets. Concrete operations of data augmentation methods are as follows:

$$\tilde{\boldsymbol{u}}_i = \boldsymbol{u}_i + G, G \sim N(0, 0.01) \tag{12}$$

$$\tilde{\boldsymbol{u}}_i = \lambda \cdot \boldsymbol{u}_i, \lambda \sim N(1, 0.01) \tag{13}$$

$$\tilde{\boldsymbol{u}}_i = \boldsymbol{u}_i \otimes \boldsymbol{M} \tag{14}$$

where $\tilde{\boldsymbol{u}}_i$ is the augmented sequence, the noise G obeys a Gaussian distribution $N(0,0.01)$, the scaling factor λ obeys a Gaussian distribution $N(1,0.01)$, the element of mask matrix $\boldsymbol{M}$ obeys a Bernoulli distribution and $\otimes$ stands for the element-wise multiplication. Besides, the above methods are carried out with the augmentation probability of 0.5.

Encoder (·): The contrastive pre-training strategy is able to select a backbone network flexibly as the fault feature encoder according to various downstream tasks. To balance the model complexity and feature extraction ability at low sampling rates, the residual network proposed in [34] is chosen as the encoder in this paper and pre-trained by the supervised contrastive learning strategy [35]. Then, high-dimensional features from this encoder are fed into the *Proj* (·) which includes a fully-connected layer and an l_2 normalization layer for the feature distance measurement.

$L_{\mathrm{sc}}(\cdot)$: In order to encourage the encoder to extract fault representations with higher intra-class similarity and inter-class dissimilarity at low sampling rates, a supervised contrastive loss is calculated as (15).

This article has been accepted for publication in a future issue of this journal, but has not been fully edited. Content may change prior to final publication. Citation information: DOI: 10.1109/TIE.2025.3572980, IEEE Transactions on Industrial Electronics

$$L_{sc}(\cdot)=\sum_{i\in I}-\log\frac{1}{|P(i)|}\sum_{p\in P(i)}\frac{\exp(z_i\bullet z_p/\tau)}{\sum_{a\in A(i)}\exp(z_i\bullet z_a/\tau)} \tag{15}$$

where $\tau\in R^+$ is a scalar temperature parameter, the anchor feature $z_i=Proj\ (Encoder\ (\tilde{u}_i))$, z_p is the positive feature of z_i, z_a is a feature from the set which not containing z_i, $a\in A(i)$ is the index of z_a, $p\in P(i)$ is the index of all positive features, $|P(i)|$ is the cardinality of all positives.

C. Diagnostic Classifier Learning Branch

Set the ISCF diagnosis as a binary classification task. Raw inputs of space voltage vector datasets are fed to $PK(\cdot)$, taking full use of the prior knowledge. Then, encoder parameters pre-trained by contrastive representation learning are frozen and transferred to match the downstream task of ISCF diagnosis. Besides, a hybrid loss function is applied to improve the classification accuracy at low sampling rates, formulated as (16).

$$L_{hybrid}(\cdot)=\beta L_{sc}(\cdot)+(1-\beta)L_{ce}(\cdot) \tag{16}$$

where this hybrid loss $L_{hybrid}(\cdot)$ is the linear combination of the supervised contrastive loss $L_{sc}(\cdot)$ and the cross-entropy loss $L_{ce}(\cdot)$. And β represents the penalty coefficient.

Afterwards, a linear classifier module $Clf(\cdot)$, including a fully-connected network and a softmax layer, is adopted to give final diagnosis results under low sampling rate scenarios.

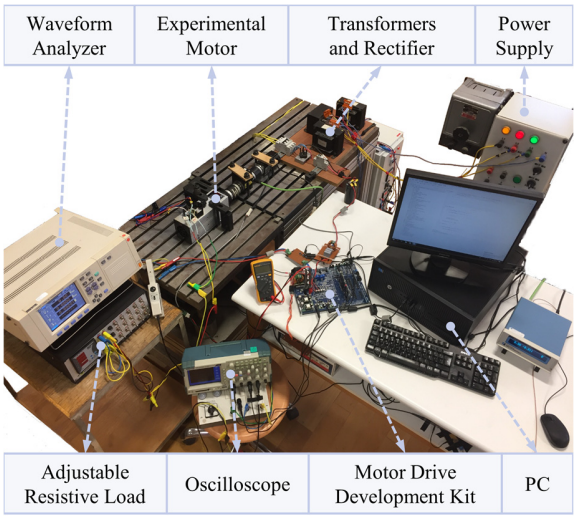

Fig. 6. Experimental platform of a closed-loop motor drive.

IV. Case Studies

In this section, space voltage vector datasets collected from a closed-loop motor drive platform are implemented to evaluate the diagnostic accuracy of incipient ISCFs at low sampling rates. Moreover, the diagnosis results of proposed method are compared with several advanced diagnosis methods under an industrial low sampling rate scenario.

A. Data Description

As shown in Fig. 6, the electrical fault diagnosis for incipient ISCFs is conducted in a closed-loop motor drive development platform [16]. This motor drive system realizes an incipient ISCF by shorting the lead points of 2 turns in the A-phase coil of an experimental motor, corresponding to around 1.92% short circuit ratio. Besides, a motor microcontroller and a 2L-VSI are integrated into a development kit of TMDXIDDK379D from Texas Instruments. The design parameters of the experimental motor are given in Table I.

TABLE I
Design Parameters of the Experimental Motor

Parameter	Value	Parameter	Value
Apparent power	640 VA	Magnetizing inductance	98 mH
Stator current	2.9 A	Stator resistance	2.3 Ω
Stator voltage	128 V	Rotor resistance	3.1 Ω
Max frequency	75 Hz	Number of pole pairs	2
Flux linkage	0.3 Wb	Number of turns per phase	104

This platform opens an interactive interface to acquire space voltage vector datasets. As tabulated in Table II, a total of 34 space voltage vector datasets are acquired at healthy and faulty states under six working conditions. For each dataset, the original sampling rate of space voltage vectors is set to be 40 kHz and 22000 elements are recorded every 0.55 seconds. However, it is difficult to extract space voltage vectors from a motor controller at a high sampling rate of 40 kHz in engineering practice. To match the real industrial scene with a low sampling rate of 1 kHz, a down-sampling operation is further carried out.

TABLE II
Dataset Description of Space Voltage Vectors

Working condition	Rotating speed/ Load torque	Training datasets	Testing datasets	High sampling rate	Low sampling rate
Case 1	1500 rpm/ 0.3 N·m	H:1 F:1	H:1 F:1	40 kHz	1 kHz
Case 2	2250 rpm/ 0.3 N·m	H:2 F:2	H:1 F:1	40 kHz	1 kHz
Case 3	2250 rpm/ 1.25 N·m	H:2 F:2	H:1 F:1	40 kHz	1 kHz
Case 4	3750 rpm/ 0.3 N·m	H:2 F:2	H:1 F:1	40 kHz	1 kHz
Case 5	3750 rpm/ 1.25 N·m	H:2 F:2	H:1 F:1	40 kHz	1 kHz
Case 6	4500 rpm/ 0.3 N·m	H:2 F:2	H:1 F:1	40 kHz	1 kHz

B. Experimental Setup

1) Network Configuration: The hyperparameters are tuned by cross-validations in training datasets, and the final results are listed in Table III. Concretely, trainable weights and biases of PK-CDM are updated iteratively, utilizing SGD optimizer with a mini-batch size of 128. The initial learning rate and weight decay are set to be 0.05 and 0.0005 respectively. After 50 training epochs, the best diagnosis model is utilized to recognize the incipient ISCF in testing datasets.

TABLE III
Hyperparameter Settings

Hyperparameter	Value	Hyperparameter	Value
Mini-batch size	128	Max epochs	50
Learning rate	0.05	Weight decay	0.0005
Optimizer	SGD	Momentum coefficient	0.9
Penalty coefficient	0.5	Temperature coefficient	0.1

2) SOTA Methods and Metrics: To demonstrate the superiority of proposed PK-CDM at low sampling rates, several SOTA methods are selected for a comprehensive comparison.

This article has been accepted for publication in a future issue of this journal, but has not been fully edited. Content may change prior to final publication. Citation information: DOI: 10.1109/TIE.2025.3572980, IEEE Transactions on Industrial Electronics

TABLE IV
DESCRIPTIONS OF METHODS USED IN THE COMPARISON

Method	Description	Category
Baseline [16]	Convolutional neural network	Deep learning
TNN [36]	Transformer neural network	
DCA-BiGRU [37]	Recurrent neural network with attention mechanism	
CCQNet [38]	Quadratic neural network with contrastive loss	Contrastive learning
PKIN (Ours)	Prior knowledge integrated convolutional neural network	Deep learning with prior knowledge
PK-CDM (Ours)	Proposed method	Contrastive learning with prior knowledge

As shown in Table IV, the baseline method with a convolutional neural network (CNN) [16], the transformer neural network (TNN) [36] and the bidirectional gated recurrent neural network with dual attention mechanism (DCA-BiGRU) [37] represent three mainstream deep learning models for fault diagnosis. The class-weighted supervised contrastive learning quadratic network (CCQNet) [38] is the novel implementation of contrastive learning for fault diagnosis. The PKIN incorporates our proposed prior knowledge integration subnetwork into a residual CNN framework. In following studies, recognition accuracy (Acc), F1-score (F1) and Matthews correlation coefficient (MCC) are used to assess the diagnosis ability comprehensively. To reduce the impact of randomness, the results of each evaluation metric are calculated ten times.

C. Performance Analysis at Low Sampling Rates

In the process of fault diagnosis for closed-loop motor drives by space voltage vectors, the influence of low sampling rates is discussed experimentally. Then, the comparison with SOTA methods proves that PK-CDM is able to ensure the highest diagnosis accuracy when the sampling rate becomes low.

1) Impact of Industrial Low Sampling Rates: In the discrete sampling process of space voltage vectors from a motor controller, the duration can be characterized by their activation states during each electrical period. Taking one operation period as the unit observation interval, usage frequencies of each basic voltage vector, such as $\boldsymbol{u}_1$ and $\boldsymbol{u}_4$, are calculated by statistical quantification of their activation states. Consequently, these discrete activation states can be mathematically converted into continuous signals in Fig. 7, representing the variation of space voltage vectors during the whole operation. In Fig. 7 (a), when the ISCF occurs, there is a significant increase in the usage frequencies of $\boldsymbol{u}_1$ and $\boldsymbol{u}_4$ at a high sampling rate of 40 kHz. However, in Fig. 7 (b), it is challenging to observe this variation at a low sampling rate of 1 kHz.

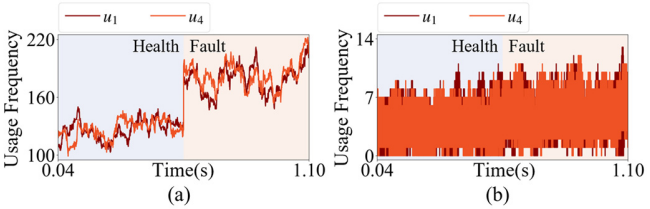

Fig. 7. Usage frequencies of space voltage vectors at various sampling rates. (a) $\boldsymbol{u}_1$ and $\boldsymbol{u}_4$ at 40 kHz. (b) $\boldsymbol{u}_1$ and $\boldsymbol{u}_4$ at 1 kHz.

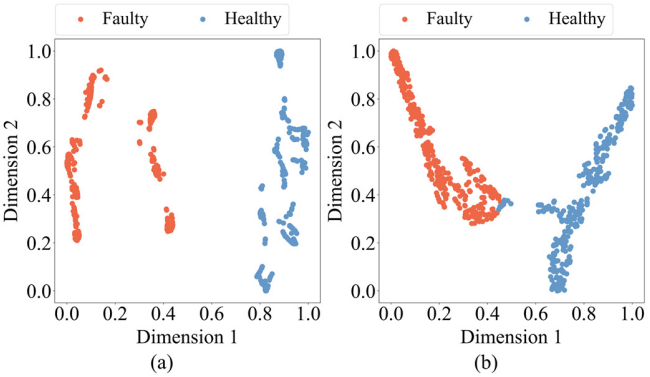

Fig. 8. Feature visualization. (a) Results at a high sampling rate of 40 kHz. (b) Results at a low sampling rate of 1 kHz.

The above observations indicate that industrial low sampling rates result in the lack of available diagnosis information, making traditional methods hard to detect the discrepancy between the health and fault state.

2) Feature Visualization at Different Sampling Rates: Space voltage vector datasets under the working condition of Case 3 are utilized to conduct the feature visualization and performance analysis of PK-CDM at different sampling rates.

Through the dimension reduction of t-distributed stochastic neighbor embedding (t-SNE), Fig. 8 shows a two-dimensional visualization of features extracted by PK-CDM under different sampling rate scenarios. In Fig. 8 (b), although there is a minimal overlap between the distribution of health and fault features, PK-CDM is still able to learn an appropriate decision-making boundary for the incipient ISCF diagnosis at a low sampling rate of 1 kHz.

3) Comparison Results with SOTA Methods: To verify the validity of PK-CDM, five SOTA methods listed in Table IV are chosen for fault diagnosis under different sampling rate conditions. Diagnosis results of comparing PK-CDM with other

TABLE V
PERFORMANCE COMPARISON RESULTS ON SPACE VOLTAGE VECTOR DATASETS UNDER DIFFERENT SAMPLING RATES

Diagnosis method	Acc		F1		MCC		Time consumption		Params
	40 kHz	1 kHz	40 kHz	1 kHz	40 kHz	1 kHz	Training	Testing	
Baseline [16]	92.81 ± 1.28	89.57 ± 1.02	92.81 ± 1.28	89.56 ± 1.50	85.79 ± 2.55	79.31 ± 2.06	455.25 ms	3.02 ms	0.1681 M
TNN [36]	92.22 ± 1.05	82.13 ± 1.60	92.22 ± 1.05	82.10 ± 1.61	84.55 ± 2.07	64.46 ± 3.18	468.12 ms	1.99 ms	0.8264 M
DCA-BiGRU [37]	95.96 ± 0.48	87.65 ± 1.87	95.96 ± 0.48	87.60 ± 1.90	92.13 ± 0.94	75.89 ± 3.55	4538.98 ms	20.95 ms	0.1791 M
CCQNet [38]	100.0 ± 0.00	91.24 ± 1.17	100.0 ± 0.00	91.17 ± 1.19	100.0 ± 0.00	83.79 ± 2.02	13975.24 ms	21.94 ms	0.7503 M
PKIN (Ours)	100.0 ± 0.00	95.85 ± 0.55	100.0 ± 0.00	95.84 ± 0.55	100.0 ± 0.00	92.03 ± 1.02	1846.16 ms	12.97 ms	0.2438 M
PK-CDM (Ours)	**100.0 ± 0.00**	**98.89 ± 0.42**	**100.0 ± 0.00**	**98.89 ± 0.42**	**100.0 ± 0.00**	**97.81 ± 0.81**	**5032.95 ms**	**14.96 ms**	**0.2673 M**

The format of results (%) is average value ± standard deviation.

This article has been accepted for publication in a future issue of this journal, but has not been fully edited. Content may change prior to final publication. Citation information: DOI: 10.1109/TIE.2025.3572980, IEEE Transactions on Industrial Electronics

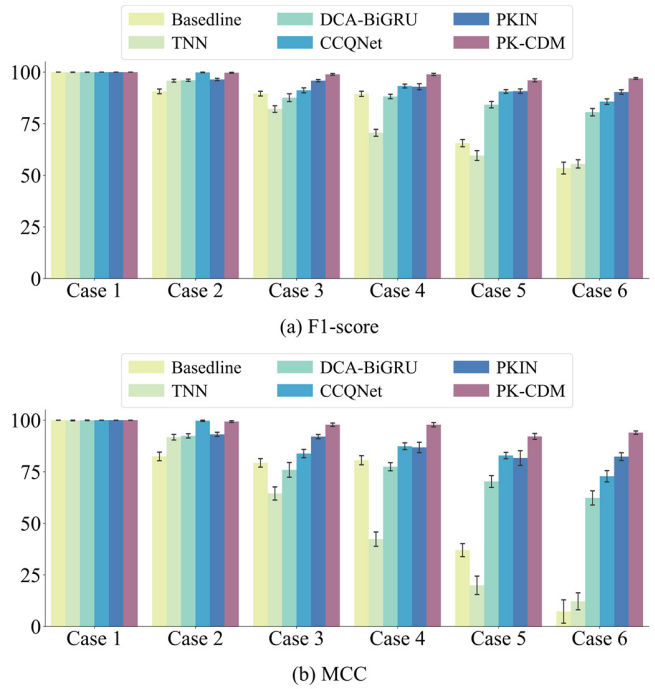

Fig. 9. Comparison results of our proposed method and other SOTA methods under different working conditions. (a) F1-score. (b) MCC.

methods are summarized in Table V. Theses comparison results denoted that the PK-CDM outperforms other methods under all the sampling rate conditions. More specifically, compared with three deep learning methods without prior knowledge, i.e., the baseline method, TNN, and DCA-BiGRU, the PK-CDM obtained higher diagnosis accuracy with the smallest deviation. Moreover, the results of PKIN revealed that with the integration of the prior knowledge module, fault diagnosis precision can be improved at low sampling rates, without requiring the complex diagnosis model design. This validated that the proposed prior knowledge module is unaffected by the reduction in sampling rates, effectively compensating for fault information loss at low sampling rates. Additionally, it can be found that contrastive learning-based methods outperform classical deep learning methods under low sampling rate conditions. This is attributed to the design of data augmentation and contrastive loss within the contrastive learning framework, which enhances the ability to extract features with useful fault representation information even at low sampling rates.

Notably, our proposed PK-CDM does not significantly increase the computational consumption for completing a single diagnostic task in Table V. Although our contrastive learning mechanism increases the offline training time per epoch, the short testing time denoted that PK-CDM is able to achieve online fault diagnosis within one operation cycle. And parameter counts of PKIN and PK-CDM indicated that the proposed prior knowledge integrated module and contrastive learning mechanism do not require excessive memory usage during the model operation. Therefore, the PK-CDM is able to ensure the highest accuracy at industrial low sampling rates and satisfy the requirement of real industrial applications.

D. Adaptability Analysis at Various Working Conditions

Given the complex working conditions encountered in engineering practice, an adaptability analysis of the proposed method under complex operational scenarios was conducted at an industrial low sampling rate of 1 kHz.

TABLE VI
PERFORMANCE ESTIMATION RESULTS OF ABLATION EXPERIMENT

Version	Acc	F1	MCC	Time consumption		Params
				Training	Testing	
1	88.06 ± 0.99	87.88 ± 1.03	78.39 ± 1.66	1819.70 ms	12.96 ms	0.2441 M
2	90.43 ± 1.05	90.34 ± 1.07	82.32 ± 1.88	1846.16 ms	12.97 ms	0.2438 M
3	90.33 ± 0.94	90.24 ± 0.97	82.15 ± 1.60	4982.06 ms	13.96 ms	0.2676 M
Ours	96.96 ± 0.41	96.96 ± 0.41	93.97 ± 0.81	5032.95 ms	14.96 ms	0.2673 M

The comparison results across different working conditions are illustrated in Fig. 9. In scenarios involving low rotational speed and light load torque, such as Case 1 and Case 2, PK-CDM and other methods achieved satisfactory diagnostic performance at the 1 kHz sampling rate. However, as rotational speed and load torque increased, the F1-score and MCC for other methods showed a marked decline. On the one hand, the negative effect of low sampling rates on fault diagnosis can be amplified by the high rotational speed. Under low sampling rate conditions, the increased rotational speed causes a proportional reduction in available space voltage vectors within a single sampling period, exacerbating the loss of useful information. On the other hand, the increased load torque also aggravates the fluctuation in monitoring signals, further masking signal variations caused by incipient ISCFs. Consequently, it is hard for conventional fault diagnosis methods to extract useful fault features at an industrial low sampling rate, especially under complex working conditions.

In contrast, our PK-CDM demonstrated the capability to extract valuable features and maintain acceptable diagnostic accuracy even under extreme operational scenarios, as observed in Case 5 and Case 6. The reason is that the proposed prior knowledge, which is not affected by working conditions, can be employed to guide signal fusion and amplify signal variations induced by incipient ISCFs. The results of PKIN also revealed that the prior knowledge module can ensure the fault diagnosis precision under complex working conditions. Moreover, with the assistance of our contrastive learning mechanism, the PK-CDM is able to extract invariant fault features to further improve the robustness of complex working conditions, thereby achieving the best diagnostic results across all tested scenarios.

This adaptability analysis across various working conditions confirms that the diagnostic accuracy of PK-CDM is not only superior but also more stable compared to other advanced fault diagnosis methods operating at an industrial low sampling rate.

E. Ablation Studies of Proposed Method

To evaluate the effectiveness of the submodules within PK-CDM for addressing closed-loop motor drive diagnosis at an industrial low sampling rate, an ablation experiment was conducted using the datasets from Case 6. In this experiment, three different versions of the model were tested. Version 1 utilized only the backbone network of PK-CDM as a diagnostic model. Version 2 incorporated the prior knowledge integrated

submodule (PKIS) in combination with Version 1. In Version 3, a contrastive pre-training strategy (CPS) was added to Version 1. Performance results are listed in Table VI.

PK-CDM demonstrated the highest diagnostic accuracy, F1-score, and MCC, with minimal deviations at a low sampling rate of 1 kHz. The results from Version 1 indicated that, under an industrial low sampling rate scenario, a residual network serves effectively as the backbone network for PK-CDM. As shown in Table VI, incorporating the enhanced components of PKIS and CPS significantly improves diagnostic accuracy at the 1 kHz sampling rate. Meanwhile, the reduction of Params in Version 2 revealed that the PKIS is able to decrease model channels and related parameters. Version 3 also denoted that the CPS only moderately rises offline training time consumption, with minimal impact on the inference time of online fault diagnosis and the storage requirement for model deployment. Thus, by integrating PKIS and CPS, PK-CDM is capable of capturing more diagnostic information to ensure diagnostic accuracy at an industrial low sampling rate, without significantly increasing time complexity and space complexity of diagnosis model in practical applications.

V. Conclusion

In this paper, the PK-CDM method has been introduced to achieve ISCF diagnosis in closed-loop motor drives at an industrial low sampling rate. In PK-CDM, space voltage vectors from a motor controller have been utilized as input signals to avoid the negative effects of closed-loop control. Additionally, PK-CDM has formulated the physical variation regularity of space voltage vectors as a prior knowledge subnetwork and has established a contrastive pre-training strategy to extract discriminative features suitable for industrial low sampling rate scenarios. The proposed PK-CDM has been experimentally validated using datasets of space voltage vectors acquired from a closed-loop motor development platform. The results have demonstrated that PK-CDM provides superior diagnostic results compared to other advanced methods at an industrial low sampling rate and that its diagnostic accuracy remains more stable under different working conditions. Furthermore, the ablation study of PK-CDM has shown that each improved submodule plays a crucial role in enhancing diagnosis accuracy under industrial low sampling rate scenarios.

For future improvements, the prior knowledge of interior control signals will be integrated with other non-invasive signals to achieve fault diagnosis for closed-loop motor drives under complex, time-varying operational conditions.

References

[1] S. Choi et al., "Fault diagnosis techniques for permanent magnet ac machine and drives—a review of current state of the art," *IEEE Trans. Transp. Electrif.*, vol. 4, no. 2, pp. 444-463, Jun. 2018.

[2] M. Zafarani et al., "Interturn short-circuit faults in permanent magnet synchronous machines: An extended review and comprehensive analysis," *IEEE J. Emerg. Sel. Top. Power Electron.*, vol. 6, no. 4, pp. 2173-2191, Dec. 2018.

[3] W. Huang et al., "Interturn short-circuit fault diagnosis of interior permanent magnet synchronous motor for electric vehicle based on search coil," *IEEE Trans. Power Electron.*, vol. 38, no. 2, pp. 2506-2515, Feb. 2023.

[4] S. Cheng, P. Zhang, and T. G. Habetler, "An impedance identification approach to sensitive detection and location of stator turn-to-turn faults in a closed-loop multiple-motor drive," *IEEE Trans. Ind. Electron.*, vol. 58, no. 5, pp. 1545-1554, May. 2011.

[5] L. Zarri et al., "Fault detection based on closed-loop signals for induction machines," in *Proc. IEEE Workshop on Elect. Mach. Des.*, *Control Diagnosis*, Mar. 2015, pp. 261-270.

[6] Y. Gritli et al., "Closed-loop control impact on the detectability of stator high-resistance connection in doubly-fed WRIMs based on rotor power spectral analysis," in *Proc. IEEE Workshop on Elect. Mach. Des.*, *Control Diagnosis*, Apr. 2017, pp. 238-243.

[7] V. Gurusamy et al., "A stray magnetic flux-based robust diagnosis method for detection and location of interturn short circuit fault in PMSM," *IEEE Trans. Instrum. Meas.*, vol. 70, pp. 1-11, 2021.

[8] H. H. Eldeeb, A. Berzoy, and O. Mohammed, "Stator fault detection on DTC-driven IM via magnetic signatures aided by 2-D FEA co-simulation," *IEEE Trans. Magn.*, vol. 55, no. 6, pp. 1-5, Jun. 2019.

[9] J. Hang et al., "Interturn fault diagnosis for model-predictive-controlled-PMSM based on cost function and wavelet transform," *IEEE Trans. Power Electron.*, vol. 35, no. 6, pp. 6405-6418, Jun. 2020.

[10] Z. Jia et al., "An MPC-based online interturn fault diagnosis method for induction motors with fault localization," *IEEE Trans. Transp. Electrif.*, vol. 11, no. 1, pp. 75-85, Feb. 2025.

[11] B. Sen, and J. Wang, "Stator interturn fault detection in permanent-magnet machines using PWM ripple current measurement," *IEEE Trans. Ind. Electron.*, vol. 63, no. 5, pp. 3148-3157, May. 2016.

[12] M. Wolkiewicz et al., "Online stator interturn short circuits monitoring in the DFOC induction-motor drive," *IEEE Trans. Ind. Electron.*, vol. 63, no. 4, pp. 2517-2528, Apr. 2016.

[13] N. Torabi et al., "On-line fault diagnosis of multi-phase drives using self-recurrent wavelet neural networks with adaptive learning rates," in *Proc. IEEE Appl. Power Electron. Conf. Expo.*, Mar. 2017, pp. 570–577.

[14] S. Huang et al., "Robust stator winding fault detection in PMSMs with respect to current controller bandwidth," *IEEE Trans. Power Electron.*, vol. 36, no. 5, pp. 5032-5042, May. 2021.

[15] Ş. İ, and O. Keysan, "Model predictive controller utilized as an observer for inter-turn short circuit detection in induction motors," *IEEE Trans. Energy Convers.*, vol. 36, no. 2, pp. 1449-1458, Jun. 2021.

[16] M. U. Oner, Ş. İ, and O. Keysan, "Neural networks detect inter-turn short circuit faults using inverter switching statistics for a closed-loop controlled motor drive," *IEEE Trans. Energy Convers.*, vol. 38, no. 4, pp. 2387-2395, Dec. 2023.

[17] Y. Oh et al., "A deep transferable motion-adaptive fault detection method for industrial robots using a residual–convolutional neural network," *ISA Trans.*, vol. 128, pp. 521-534, Sep. 2022.

[18] I. Lee et al., "System-level fault diagnosis for an industrial wafer transfer robot with multi-component failure modes," *Appl. Sci.*, vol. 13, no. 18, pp. 10243. 2023.

[19] B. Ayhan et al., "On the use of a lower sampling rate for broken rotor bar detection with DTFT and AR-based spectrum methods," *IEEE Trans. Ind. Electron.*, vol. 55, no. 3, pp. 1421-1434, Mar. 2008.

[20] H. Keskes et al., "Broken rotor bar diagnosis in induction machines through stationary wavelet packet transform and multiclass wavelet SVM," *Electr. Power Syst. Res.*, vol. 97, pp. 151-157, 2013.

[21] S. Zhao, F. Blaabjerg and H. Wang, "An Overview of Artificial Intelligence Applications for Power Electronics," *IEEE Trans. Power Electron.*, vol. 36, no. 4, pp. 4633–4658, Apr. 2021.

[22] S. Yang et al., "Industrial Battery State-of-Health Estimation with Incomplete Limited Data Toward Second-Life Applications," *JDMD*, vol. 3, no. 4, pp. 246–257, Jul. 2024.

[23] X. Li et al., "Dynamic vision-based machinery fault diagnosis with cross-modality feature alignment," *IEEE/CAA J. Autom. Sin.*, vol. 11, no. 10, pp. 2068–2081, Oct. 2024.

[24] W. Zhang, H. Hao, and Y. Zhang, "State of charge prediction of lithium-ion batteries for electric aircraft with swin transformer," *IEEE/CAA J. Autom. Sin.*, pp. 1-3. 2024.

[25] W. Zhang and X. Li, "Federated transfer learning for intelligent fault diagnostics using deep adversarial networks with data privacy," *IEEE/ASME Trans. Mechatron.*, vol. 27, no. 1, pp. 430–439, Feb. 2022.

[26] T. Zhang et al., "Series AC arc fault diagnosis based on data enhancement and adaptive asymmetric convolutional neural network," *IEEE Sens. J.*, vol. 21, no. 18, pp. 20665-20673, Mar. 2021.

[27] J. Chen et al., "A novel knowledge sharing method for rolling bearing fault detection against impact of different signal sampling frequencies," *IEEE Trans. Instrum. Meas.*, vol. 72, pp. 1-12, 2023.

This article has been accepted for publication in a future issue of this journal, but has not been fully edited. Content may change prior to final publication. Citation information: DOI: 10.1109/TIE.2025.3572980, IEEE Transactions on Industrial Electronics

[28] J. Hang et al., "Online interturn fault diagnosis of permanent magnet synchronous machine using zero-sequence components," *IEEE Trans. Power Electron.*, vol. 30, no. 12, pp. 6731-6741, Dec. 2015.
[29] J. Li et al., "Fault signal propagation through the PMSM motor drive systems," *IEEE Trans. Ind. Appl.*, vol. 53, no. 3, pp. 2915-2924, May/Jun. 2017.
[30] Y. Yao, Y. Li, and Q. Yin, "Bandpass effect and its compensation method for diagnosis in a closed-loop control system," *IEEE-ASME Trans. Mechatron.*, vol. 25, no. 3, pp. 1679-1689, Jun. 2020.
[31] G. A. Orcajo et al., "Diagnosis of electrical distribution network short circuits based on voltage park's vector," *IEEE Trans. Power Deliv.*, vol. 27, no. 4, pp. 1964-1972, Oct. 2012.
[32] I. F. El-Arabawy, M. I. Masoud, and A. E. K. Mokhtari, "Stator inter-turn faults detection and localization using stator currents and concordia patterns - neural network applications," in *Proc. Compat. Power Electron.*, May. 2007, pp. 1–6.
[33] T. Peng et al., "Fault feature extractor based on bootstrap your own latent and data augmentation algorithm for unlabeled vibration signals," *IEEE Trans. Ind. Electron.*, vol. 69, no. 9, pp. 9547-9555, Sep. 2022.
[34] K. He et al., "Deep residual learning for image recognition," in *Proc. IEEE Conf. Comput. Vis. Pattern Recognit. (CVPR)*, Jun. 2016, pp. 770–778.
[35] Y. S. Cho, and S. B. Kim, "Supervised contrastive learning for multisensor signals classification in automobile engine manufacturing," *IEEE Trans. Ind. Inform.*, vol. 20, no. 5, pp. 7764-7776, Feb. 2024.
[36] F. Parvin et al., "A comprehensive interturn fault severity diagnosis method for permanent magnet synchronous motors based on transformer neural networks," *IEEE Trans. Ind. Inform.,* vol. 19, no. 11, pp. 10923-10933, Feb. 2023.
[37] X. Zhang et al., "Fault diagnosis for small samples based on attention mechanism," *Measurement*, vol. 187, Jan. 2022, Art. no. 110242.
[38] W. Yu et al., "A class-weighted supervised contrastive learning long-tailed bearing fault diagnosis approach using quadratic neural network," 2023, *arXiv: 2309.11717*.

Jinze Jiang received the M.S. degree in aeronautical engineering from Northwestern Polytechnical University, Xi'an, China, in 2021. He is currently pursuing the Ph.D. degree in mechanical engineering at the Key Laboratory of Education Ministry for Modern Design and Rotor-Bearing System, Xi'an Jiaotong University, Xi'an, China.

His research interests include condition monitoring and electrical faut diagnosis of motor drives.

Yaguo Lei (M'15-SM'19) received the B.S. and Ph.D. degrees in mechanical engineering from Xi'an Jiaotong University, P.R. China, in 2002 and 2007, respectively. He is currently a Full Professor of mechanical engineering at Xi'an Jiaotong University. Prior to joining Xi'an Jiaotong University in 2010, he was a Postdoctoral Research Fellow with the University of Alberta, Canada. He was also an Alexander von Humboldt Fellow with the University of Duisburg-Essen, Germany.

His research interests include machinery condition monitoring and intelligent maintenance, dynamic modeling, signal processing, intelligent fault diagnosis, and remaining useful life prediction. He has pioneered many fault diagnosis and prognosis methods, and applied them to industrial areas, such as wind turbines, trains and industrial robots, etc.

Dr. Lei is a fellow of ASME, IET and ISEAM, a senior member of Chinese Mechanical Engineering Society, Operations Research Society of China and Chinese Association of Automation, respectively. He is currently an associate editor or editorial board member of more than ten journals, including IEEE Transactions on Industrial Electronics and Mechanical Systems and Signal Processing.

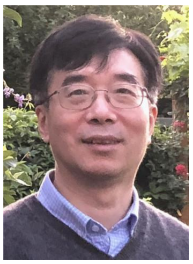

Zidong Wang (Fellow, IEEE) was born in Jiangsu, China, in 1966. He received the B.Sc. degree in mathematics from Suzhou University, Suzhou, China, in 1986, and the M.Sc. degree in applied mathematics and the Ph.D. degree in electrical engineering from Nanjing University of Science and Technology, Nanjing, China, in 1990 and 1994, respectively.

From 1990 to 2002, he held teaching and research appointments in universities in China, Germany, and the United Kingdom. He is currently a Professor of dynamical systems and computing with the Department of Computer Science, Brunel University London, Uxbridge, U.K. He has published more than 600 articles in international journals. His research interests include dynamical systems, signal processing, bioinformatics, control theory, and applications.

Prof. Wang is a member of the Academia Europaea and European Academy of Sciences and Arts, an Academician of the International Academy for Systems and Cybernetic Sciences, a fellow of the Royal Statistical Society, and a member of the Program Committee of many international conferences. He holds the Alexander von Humboldt Research Fellowship of Germany, the JSPS Research Fellowship of Japan, and the William Mong Visiting Research Fellowship of Hong Kong. He serves (or has served) as the Editor in-Chief for International Journal of Systems Science, Neurocomputing, and Systems Science and Control Engineering. He serves as an Associate Editor for 12 international journals, including IEEE TRANSACTIONS ON AUTOMATIC CONTROL, IEEE TRANSACTIONS ON CONTROL SYSTEMS TECHNOLOGY, IEEE TRANSACTIONS ON NEURAL NETWORKS AND LEARNING SYSTEMS, IEEE TRANSACTIONS ON SIGNAL PROCESSING, and IEEE TRANSACTIONS ON SYSTEMS, MAN, AND CYBERNETICS—Part C: Applications and Reviews.

Ke Feng (Member, IEEE) received the Ph.D. degree from the University of New South Wales, Sydney, NSW, Australia, in 2021. He worked at the University of British Columbia, Vancouver, BC, Canada, and the National University of Singapore, Singapore, in 2022 and 2023, respectively. He is a Full Professor at Xi'an Jiaotong University, Xi'an, China. His main research interests include digital twins, vibration analysis, structural health monitoring, dynamics, tribology, signal processing, and machine learning. Dr. Feng is a Marie Curie Fellow (Imperial College London and Brunel University London). He was recognized as the Emerging Leader in 2023 by the Measurement Science and Technology journal. He is an Associate Editor and a Guest Editor of several journals, including IEEE TRANSACTIONS on INDUSTRIAL INFORMATICS (TII), Mechanical Systems and Signal Processing (MSSP), Journal of Intelligent Manufacturing (JIM), Structural Health Monitoring (SHM), IEEE TRANSACTIONS ON INSTRUMENTATION AND MEASUREMENT (TIM), IEEE TRANSACTIONS ON INDUSTRIAL CYBER-PHYSICAL SYSTEMS (TICPS), Ocean Engineering and Information Fusion.

Xiaofei Liu received the M.S. degree in mechanical engineering from Dalian University of Technology, Dalian, China, in 2019. He is currently pursuing the Ph.D. degree in mechanical engineering at the Key Laboratory of Education Ministry for Modern Design and Rotor-Bearing System, Xi'an Jiaotong University, Xi'an, China.

His research interests include condition monitoring and remaining useful life prediction of machines.